Materials Advances

Accepted Manuscript

This article can be cited before page numbers have been issued, to do this please use: M. SINGH, F. Scotognella and G. M. Paternò, *Mater. Adv.*, 2024, DOI: 10.1039/D4MA00426D.

ROYAL SOCIETY OF CHEMISTRY

rsc.li/materials-advances

View Article Online
DOI: 10.1039/D4MA00426D

ARTICLE

Degenerately Doped Metal Oxide Nanocrystals for Infrared Light Harvesting: Insight Into their Plasmonic Properties and Future Perspectives

Received 00th January 20xx,
Accepted 00th January 20xx

DOI: 10.1039/x0xx00000x

Mandeep Singh,[a] Francesco Scotognella [b*] and Giuseppe Maria Paterno [a*]

The tuneability of localized surface plasmon resonace (LSPR) of degenerately doped metal oxides (MOXs) nanocrystals (NCs) over a wide range of infrared (IR) region via controlling NCs size and doping content offer a unique opportunity to develop future generation optoelectronics and photonic devices like IR photodetectors, sensors etc. The central aim of this review article is to highlight the distinct and remarkable plasmonic properties of degenerately or heavily doped-MOXs nanocrystals via reviewing comprehensive literature reported so far. Particularly, literature of each MOXs NCs i.e. ZnO, CdO, In_2O_3, and WO_3 doped with different dopants discussed separately. In addition to the discussion on most commonly used colloidal synthesis approaches, the ultrafast dynamics of charge carriers in NCs and extraction of LSPR assisted- hot carriers are also discussed in detail. Finally, the future perpective applications of MOXs NCs in IR photodetector and photovoltaic (PV) self-powered chemical sensor are also presented.

Introduction

The confinement of light at nanoscale level via LSPR offers a unique light-matter interactions[1,2] and proves to be highly efficient as it offers unique pathway to enhance the performance of many modern electronics devices such as solar cell, gas sensors, biosensors, light emitting diodes and so on. [3–8] For a long time, LSPR were assumed to be the special properties that are only associated with noble metals nanoparticles like Au, Ag etc.[1] However, beside their remarkable properties, the LSPR in noble metals is high cost pathway and offer non-tuneability due to the high and fixed density of charge carrier in metals ($\sim 10^{23}$ cm^{-3}).[1]

The discovery of LSPR in degenerately doped MOXs nanocrystals (NCs) such as aluminium doped ZnO (AZO), tin doped indium oxide (ITO), WO_3 etc., opens up a new possibility to develop future generation optoelectronic and photonics devices.[1,9,10] LSPR in doped-semiconductors holds an advantage over metal nanoparticles because their LSPR can be tuned from THz to NIR region via controlling doping level and NCs size as shown in fig. 1.[11] This is a two dimensional Drude-Lorentz plot between the NCs size vs. LSPR frequency. As it can be seen from fig. 1, for degenerately doped semiconductors, by controlling the doping concentration between 10^{19}-10^{21} cm^{-3}, the LSPR can be tuned from far infrared (FIR) to near-infrared (NIR) region. The wide range tuneability over the IR region, makes degenerately doped semiconductors interesting for optoelectronics, photonics, biomedical etc. applications. [12–14] Particularly, Furthermore, most of the MOXs such as ZnO, CdO, In_2O_3, WO_3 etc. are intrinsically n-type doped semiconductors due to the presence of oxygen vacancies, thus exhibits LSPR features even when no external doping has been done.[2] The prime example of this is the WO_{3-x} NCs.[15]

This review article is focused on highlighting the plasmonic properties of MOXs NCs via reviewing significant literature reported so far and their future perspective application in IR photodetectors and PV self-powered sensors. While reviewing the literature, we have tried to includes all those reports in which interesting synthetic conditions or strategies were used to tune and improve the plasmonic properties of MOXs NCs. We would like to point out that for a detailed and deeper understanding of different types of degenerately doped semiconducting materials and their fundamental plasmonic properties, readers can refer to comprehensive review article by Milliron and collaborators.[2] Here, we first discussed the properties which makes MOXs NCs unique material to harvesting light from a wide solar spectrum (UV-ViS-IR) and overview the ultrafast charge carrier dynamics along with the extraction of LSPR-assisted hot-carriers. Then, we present the most commonly used colloidal synthesis methods of NCs with relevant examples and review the comprehensive literature on degenerately doped indium oxide (In_2O_3), zinc oxide (ZnO), cadmium oxide (CdO) and tungsten oxide (WO_x) NCs. Finally, perspective applications of NCs in IR photodetectors and PV self-powered sensors are also presented.

[a] Physics Department, Politecnico di Milano, Piazza L. da Vinci 32, 20133 Milano (Italy)
[b] Department of Applied Science and Technology, Politecnico di Torino, Corso Duca degli Abruzzi 24, Torino, 10129, Italy
† Email: giuseppemaria.paterno@polimi.it, francesco.scotognella@polito.it

View Article Online
DOI: 10.1039/D4MA00426D

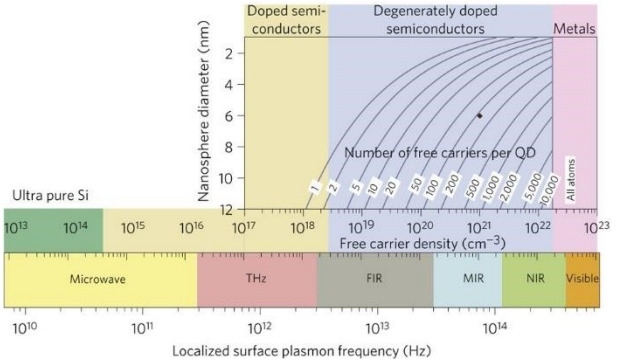

Figure 1 Localized surface plasmon resonance (LSPR) frequency dependence on free carrier density and doping constraints. Reproduced from ref. 11 with permission from Springer Nature, copyright 2011.

Observance of LSPR in IR extend light-harvesting region of wide-band gap MOXs: From UV through VIS to IR

Wide-band gap MOXs such as ZnO, TiO_2, In_2O_3 are generally transparent to visible light, with band gap in the UV-region.[16–18] Due to their strong absorption in UV, these materials are immensely explored as a UV-photodetectors[19,20] and are also employed to further enhance the efficiency of Si-solar cell by harvesting UV-light.[21] Furthermore, the band gap of MOXs can be tuned via varying the nanoparticles size and doping with different elements that provides the possibility to harvest wide-range of UV light.

Recently, it has been observed that photogeneration of charge carriers occurs in the MOXs under visible light excitation.[22] This phenomenon is significantly explored in tuning the selectivity and response of gas sensors.[22,23] Q. Geng et al.[24] have illuminated the ZnO with visible light ranging from 420nm to 520 nm from LED source and observed the sensing response owing to the photo-generated charge carriers. They have associated photogeneration in visible light with the phenomenon of two-photon or multi-photon absorption.[25,26] The detail discussion about these phenomena is out of the scope of this review.

Finally, the LSPR in heavily doped MOXs NCs in IR, which is the main topic of this review article, extends the MOXs light-harvesting capability to IR region. Later in the review article we will discuss the perspective application of MOXs NCs for future generation of IR-photodetectors and photovoltaic (PV) self-powered sensor due to ability of harvest energy form wider-range of solar spectrum (UV-ViS-IR). However, to use degenerately doped MOXs NCs for these two applications, required deeper understanding of their plasmonic dynamics under the illumination of IR-radiation and proper device configuration for plasmon-assisted hot-carrier extractions. This leads us to our next section in which both these aspects are discussed.

Ultrafast Dynamics in Degenerately doped MOXs NCs and Extraction of Hot carriers

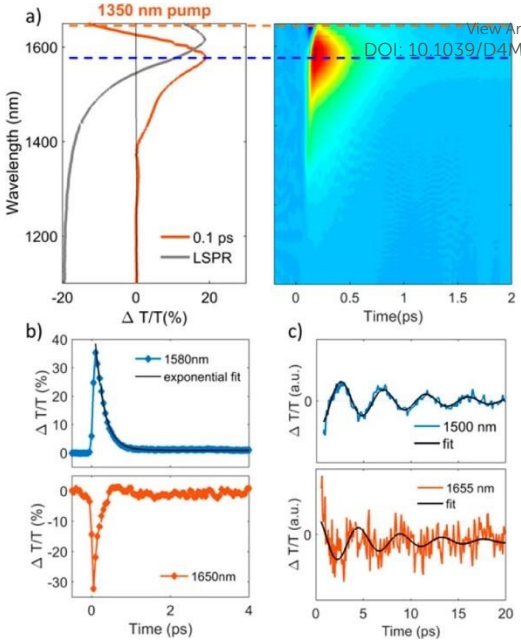

Figure 2 Transient optical response of FICO NCs following intraband excitation. (a) Representative TA spectrum at the maximum rise time around 100 fs after photoexcitation, exhibiting a derivative-shaped curve (left) together with the two-dimensional $\Delta T/T$ map (right), showing the signal as a function of pump–probe delay and probe wavelength for FICO NCs excited at 1350 nm with an excitation density 0.13 mJ/cm^2. The steady-state LSPR absorption spectrum is also given in grey for comparison. (b) Transient decay dynamics at 1580 nm together with a biexponential fit (blue and black curve, respectively; upper panel, time constants of 0.23 and 38 ps) and 1650 nm (red curve, lower panel), illustrated by the horizontal cuts (dashed lines) depicted in panel a. The time constant of the initial fast decay at 1650 nm is around 0.15 ps (not shown here). (c) $\Delta T/T$ time traces extracted at the selected probe wavelengths to the red (around 1655 nm) and the blue (1500 nm) of the maximum PB signal after subtracting the biexponential decay, along with their fits by a damped sinusoidal function (black curves). The extracted oscillating period is T = 4.4 ps, and the damping time constant is τ = 7 ps. Reproduced from ref. 36 with permission from ACS, copyright 2016.

The study of materials in different forms (gas, liquid, solid) via mean of ultrafast transient-absorption spectroscopy is of high interest as it provides useful information about the charge-carriers dynamics that occurs at very short-time scales (e.g. in femtoseconds), like plasmonic decays, plasmon induced hot-carrier dynamics, exciton formation/dissociation etc.[27–32] These types of investigations offer ultrafast signal manipulation with large transmittance variation, which is highly important for applications in active plasmonic, optical switching and all-optical signal-processing devices. [33–35]

In this regard, Kriegel et al.[36] have investigated the ultrafast photodoping and plasmons dynamics in fluorine-indium co-doped CdO (FICO) NCs via pumping at 400nm (band-gap excitation) and 1350nm (LSPR excitation). The NCs were prepared by heat-up method and the measurement were performed on the suspension of NCs in different solvents. Fig.2 represents the transient absorption (TA) response of FICO NCs to the intraband excitation of LSPR at 1350nm. Particularly, Fig.2a shows the derivative shaped TA spectra at a time-delay of 0.1ps (left) along with the two-dimensional map $\Delta T/T(\%)$ (right). Two types of contribution were observed: the maximum of TA spectra (indicated by broken blue line), represents the

View Article Online
DOI: 10.1039/D4MA00426D

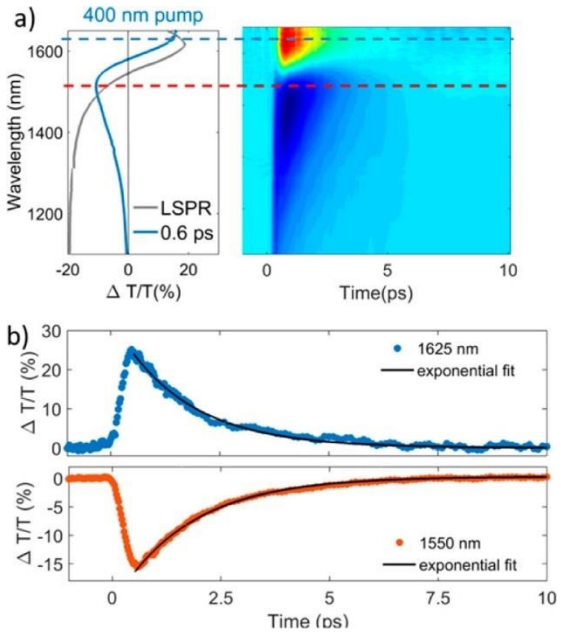

Figure 3 Transient optical response of FICO NCs following intraband excitation. (a) TA spectrum at the maximum signal (0.6 ps) showing the typical derivative-shaped curve together with the two-dimensional $\Delta T/T$ map showing the signal as a function of pump–probe delay and probe wavelength for FICO NCs excited at 400 nm for the excitation density 2.35 mJ/cm^2. The steady-state LSPR absorption spectrum is also given in gray for comparison. (b) Transient decay dynamics at 1625 nm (blue curve upper panel) and 1550 nm (red curve lower panel) together with the monoexponential fits (black curve, time constant of 1.7 ps), illustrated by the horizontal cuts (dashed lines) depicted in panel a. Reproduced from ref. 36 with permission from ACS, copyright 2016.

photobleaching (PB) and photoinduced absorption (PA) indicated by broken red line. In the fig. 2b the decay of both PB and PA at 1580nm and 1650nm were shown. Two well separated time-dependant dynamics were observed when NCs were excited with LSPR resonance: short-dynamics in picosecond time range and longer-dynamics from 10-100 of picoseconds. The initial fast decay (1ps) is associated with the emission of phonons (carrier-phonons) and slower- decay corresponds to the phonon-phonon scattering and dissipation of heat into the solvent. It was also indicated that the initial fast decay was in fact even faster than the noble metals due to the lower heat capacity and carrier concentration of semiconductor NCs. On the other hand, the TA dynamics of NCs after band-gap excitation (400nm) is shown in fig. 3. As shown in figure 3a, reverse dynamics as compared to LSPR excitation is observed. The PB maximum was observed at 1625nm, while negative signal (PA) showed peak value at 1550nm. Furthermore, the time axis in two-dimensional of LSPR excitation (fig. 2a) was up to 2ps, while 10ps in the cased on 400nm excitation, indicating the faster dynamics and signal modulation is occurred when NCS were excited at 1350nm. A monoexponentially decay in the signal was observed after the short rise time. Author argued that pumping at 400nm results into the excitation of electrons to the conduction band which increases the carrier density by capacitive charging. They have proposed that the observed mono-exponential decay is due to the temporarily increased carrier density after the ultrafast photodoping which decays via electron–hole recombination.

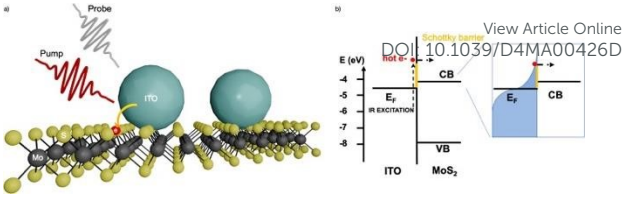

Figure 4(a) ITO/MoS_2 heterojunction sketch. (b) Band alignment between ITO and MoS_2; on the right-hand side, we have the sketch of the hot Fermi–Dirac distribution. Reproduced from ref. 39 with permission from ACS, copyright 2022.

In another work, In and Al-doped ZnO NCs were explored for ultrafast and broadband mid-infrared all-optical switching.[37]

The In-doped ZnO NCs were synthesized using heat-up methods while Al-doped ZnO NCs were synthesized using hot-injection. Briefly, via pumping NCs with LSPR resonance, picosecond all-optical Q-switching was realized with doped ZnO NCs in the MIR region from 3-5 μ m.

Furthermore, the practical use these plasmonic properties of doped- MOXs NCs relies majorly on the extraction of LSPR-assisted hot-electrons. However, hot-electrons exhibits very short life-time (tens of femtoseconds in metal[38] and 100 of femtoseconds in doped oxide NCs[36]), making it difficult to extract. The extraction of these hot-carriers requires a proper device structure or junction with suitable extracting layer. One such effort was done by M. Guizzardi et al.[39] in which the extraction of hot-carriers were done via fabricating the heterostructure between ITO NCs and monolayer of molybdenum disulfide (MoS_2). The ITO NCs were synthesized by continuous growth method and were transferred to the MoS_2 monolayer with spin-coating. Figure 4 showed the depiction of ITO/MoS2 heterojunction and band alignment between ITO and MoS_2. The heterostructure was pumped in resonance with LSPR of ITO NCs at 1750nm which was well below the band gap of MoS_2. Via pumping the LSPR, a charge transfer from ITO to MOS_2 were observed that makes these types of heterostructure interesting of light-harvesting devices like infrared-solar cell.

After discussing plasmonic dynamics in NCs, we reach a point where it is necessary discus the synthetic approaches that are used to synthesize these plasmonic materials.

Synthesis of Degenerately Doped MOXs NCs

Together with the obvious cost-effectiveness, solution-phase synthesis provides ease and flexibility to tune the LSPR over the wide range of IR-region via chemical controls over the (i) dopants incorporation inside the NCs, (ii) type of dopant and (iii) dopant concentration.[2] Among the different solution processable approaches like coprecipitation in aqueous solvents, reverse micelle templating, colloidal synthesis has gained significant attention owing to its ability to produce homogeneous NCs of many different materials including MOXs, thus dominated over other synthetic routes.

For the synthesis of plasmonic MOXs NCs, three main colloidal synthetic route routes have been immensely used, namely:

(a) Hot-injection method

(b) Heat-up method

View Article Online
DOI: 10.1039/D4MA00426D

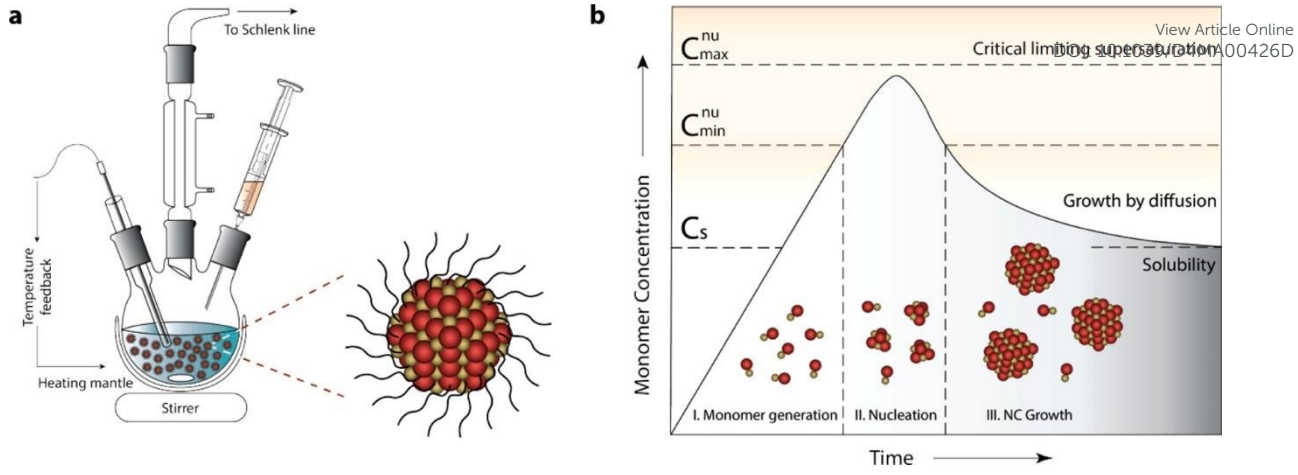

Figure 5 General synthetic apparatus and growth model embodying the colloidal synthetic technique. (a) Schematic showing glassware and peripheral instrumental setup for a typical synthesis of surfactant stabilized NCs, involving hot-injection. (b) LaMer-Dinegar model of colloidal NC formation. The three stages of monomer generation, nucleation, and growth are demarcated in the regions below the growth curve along with cartoons depicting the progression of the synthesis. Reproduced from ref. 2 with permission from ACS, copyright 2018.

(c) Continuous growth method (slow injection)

The typical experimental set-up for NC synthesis is composed of three-neck round bottom flaks, heating mantle with temperature controller (inserted into the NC solution) and syringe for the injection of the reactant. As the synthesis is done in the inert environment condition (e.g. in nitrogen), the middle neck is connected to the Schlenk line. The schematic of the set-up is shown in the fig. 5a.[2]

Before we go into the detail of these methods, it is important to understand the nucleation and growth of NCs that were explained by LaMer and Dinegar in 1950.[40] Particularly, they have investigated the development of sulphur hydrosol for the slow decomposition of dilute sodium thiosulfate in dilute hydrochloric acid. Basically, it consists of three stages: monomer generation, nucleation and finally the growth of NCs (fig.5b).[2] In the first stage, the precursor is dissolved in the solvent and the reaction between them leads to the formation of monomer.

The rate of monomer generation depends on the reaction kinetics and temperature. As the reaction proceeds, the concentration of monomer reaches its saturation level (C_s) and at this point nucleation didn't start immediately as significant barrier for the nucleation still exists. However, when monomer concentration reaches certain minimum level (C^{nu}_{min}), the nucleation spontaneously starts. During the accelerated growth of nuclei, the monomers is abruptly consumed. In fact, monomer is formed by an aggregation and self-nucleation processes. As the temporal formation of nuclei goes on, the monomer concentration reaches supersaturation and drops instantaneously. Indeed, the nucleation process stops when it reaches the C^{nu}_{min} level, which is onset of third and final stage i.e. the growth of NCs via aggregation of monomers on pre-existing nuclei.

Now, let us come back to the three NCs synthesis methods. All three methods are similar to each other as far as the overall process is concern, however the major different lies the occurrence of nucleation and growth.[2]

Hot-Injection method

The hot-injection methods was first introduced by Bawendi et al.[41] in 1993 for the synthesis of CdE NCs in which E represents the three different elements: S, Se and Te. Afterward, it was immensely used to produce high quality NCs of variety of materials including degenerately doped MOXs. As its name suggest, the precursor is quickly injected into preheated solvent maintained in inert environment under stirring. The central focus of hot-injection is to create single nucleation even after the injection with the successive growth of NCs that does not coincide with secondary nucleation. In other words, fast injection instantaneously starts the nucleation and the progression of reaction leads to the formation of NCs. The solution also contained surfactant ligand that hinders the agglomeration and determines the shape and size of NCs. Notable surfactant ligand that have been used in the synthesis of NCs are long-chain carboxylic acids (oleic acid), alkylphosphine & alkylphosphine oxides (trioctylphosphine) and long-chain amines (oleylamine). Furthermore, by variation in growth temperature and time along with the surface concentration, NCs of different sized and distribution can be achieved. In fact, as nucleation and growth occur separately, hot-injection method offers high controls over the size and size distribution of NCs.

With this method, Sirshendu Ghosh et al.[42] have fabricated indium (In) doped ZnO NCs in the nanopyramid shape as shown in fig. 6. The whole synthesis process is as follow: 2mM of Zinc acetylacetonate and indium acetate with different molar ratio is mixed with 2 mmol oleic acid and 5 ml of 1-octadecene (ODE) three neck round bottom flask. The mixture was first vacuumed at room-temperature and finally heated up to 90 °C under the flow of Ar-gas. Afterward, 15mM oleyl amine dissolved in 1ml of ODE and injected into the flask. The mixture was heated for 60 minutes at 240 C that leads to the formation of In-doped ZnO NCs with the broad LSPR in the IR-region.

This method is extremely useful for applications in which precise control over physical properties of NCs is required, i.e. exploitation of LSPR. However, hot-injection is not useful for large-scale production, due to its dependency on homogeneous mixing of reactants in a short period of time at high temperatures, cooling can be inhomogeneous if the reaction is performed in a large reactors

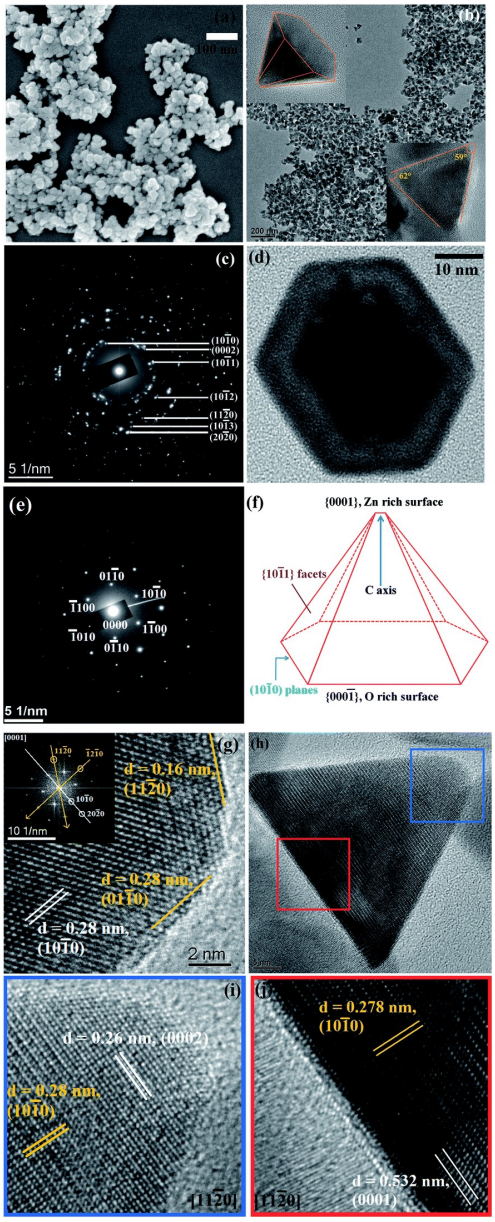

Figure 6 (a) FESEM image of pure ZnO. (b) Low resolution TEM image of the pure ZnO nanopyramid. The top-left and bottom right insets of the figure depict the tilted (X = 41.1°, Y = 0°) and side views of a single ZnO hexagonal nanopyramid. (c) SAED pattern of the nanopyramid. (d) A single hexagonal pyramid viewed from the (0001) zone axis. (e) SAED pattern of the single nanocrystal. (f) Schematic presentation of a nanopyramid. (g) HRTEM image of a nanocrystal at the cross-section of two edges of base. The inset shows the corresponding FFT pattern of the area. (h) Side view of a nanopyramid. (i) HRTEM image of the tip of the pyramid. (j) HRTEM image of the base of the pyramid. Reproduced from ref. 42 with permission from RSC, copyright 2014.

and large volume of reactant cannot be injected abruptly that can leads to the fabrication of inhomogeneous NCs with broad sizes.[2]

Heat-up method

Unlike hot-injection, heat-up is a non-injection method that involves the slow or steady heating of precursor in the presence of ligand. This method was first introduced by Hyeon et al.[43] in 2001 as an alternating to hot-injection, in which they have synthesized monodispersed iron oxide nanoparticles. The experimental set-up

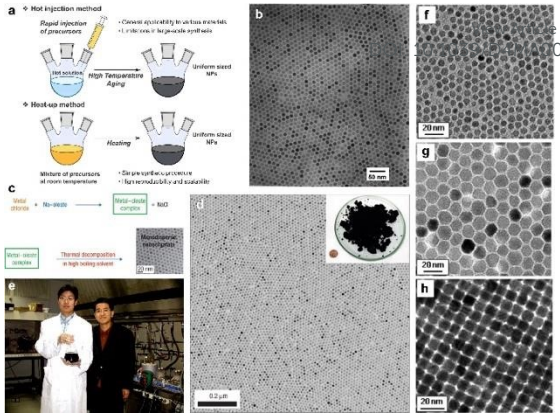

Figure 7 a) Schematic illustration of hot injection method and heat-up method for uniform-sized nanoparticles. b) Transmission electron microscopy (TEM) image of 11 nm γ-Fe_2O_3 nanoparticles. c) The overall scheme for the synthesis of monodisperse nanoparticles through metal-oleate complexation. d) TEM image of 12 nm Fe_3O_4 nanoparticles. Inset is a photograph of 40 g of the monodisperse Fe_3O_4 nanoparticles, and a US one-cent coin for comparison. e) Photograph of Taeghwan Hyeon and Jongnam Park in 2004. f-h) TEM images of (f) 6 nm, (g) 12 nm, (h) 10 nm monodisperse Fe_3O_4 nanoparticles. Reproduced from ref. 44 with permission from Wiley, copyright 2023.

that described the process of nanoparticles growth in comparison to hot-injection method (fig 7a), the scheme to synthesized nanoparticles (fig. 7c), picture of Taeghwan Hyeon and Jongnam Park (fig.7e) and TEM images of iron oxide nanoparticles with different sizes are shown in fig. 7 (b, d, f-h).[44] As shown in fig. 7a, the mixture of precursor, surfactants and solvents is heated to first initiate the nucleation and then the growth of NCs. Hyeon et al.[43] have done the decomposition of iron pentacarbonyl in the presence of oleic acid at 100 °C that leads to the generation of iron−oleic acid metal complex. This metal complex then further heated up to 300 °C (aging) that eventually forms the iron nanoparticles. To oxidize these iron NCs to form iron oxide NCs, the trimethylamine oxide is added into the mixture as an oxidant agent. In the heat-up method, the nucleation step last longer than hot-injection because of the continue generation of monomers caused by the sustained supply of heat. This leads to the overlap between nucleation and growth stage: in fact, additional nucleation can also happen during the growth of initial nuclei. Hence, the control over high degree of size and shape is sometime difficult with this method, due to the overlap between nucleation and growth stages. The main advantage of heat-up method is its scalability, as no-injection step is involved and all the reactants are mixed up and heated together to generate high quality NCs.

Continuous Growth Method

In a continuous growth method, the precursor is slowly injected into the solution pre-heated at certain temperature. Hence, this method is an intermediate between hot-injection and heat-up methods. The slow and continuous injection of precursor allows the growth of well-sized and uniform NCs because of the layer-by

layer deposition of monomer on the NCs surface. Hence, this method is useful to synthesize core-shell NCs, in which core and shell is made-up of different materials like CdSe/ZnS core-shell NCs. Via using this method, Fe, Co, Cu and Zn doped In_2O_3 NCs

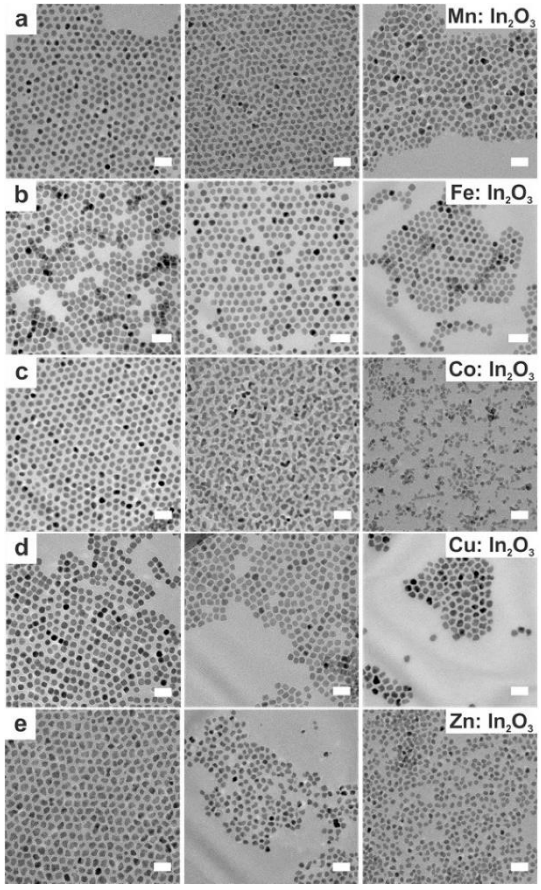

Figure 8 TEM images taken of doped In_2O_3 nanocrystals at varying molar dopant ratios. Scale bars are 20 nm. The nominal dopant percent in the precursor increases from left to right, 5% dopant on the left, 10% center, and 20% right. (a) displays Mn:In_2O_3, (b) Fe:In_2O_3, (c) Co:In_2O_3, (d) Cu:In_2O_3, and (e) Zn:In_2O_3. Reproduced from ref. 45 with permission from ACS, copyright 2017.

were synthesized.[45] Briefly, metal-oleate precursor was prepared by mixing 1mM indium(III) acetate and specific amount of dopant precursors in 2ml oleic acid in a vial which is then heated at 150 °C in an oil bath under N_2 environment for 1 hour. In the case of doping with Fe, the heating was done at 190°C. After the completion of reaction, this solution was slowly injected (0.35 mL/min) to 13ml of oleyl alcohol and heated to 290 °C under N_2 environment. The TEM images of doped In_2O_3 NCs are shown in figure 8.

Progress in the MOXs NCs

After the discussion on synthetic approaches, now will review the literature of different MOXs NCs and explore their plasmonic properties. . Particularly, we will focus on how different experimental conditions or strategies like the use of different dopants, doping levels, temperature of growth etc. can influence their LSPR in the IR region.

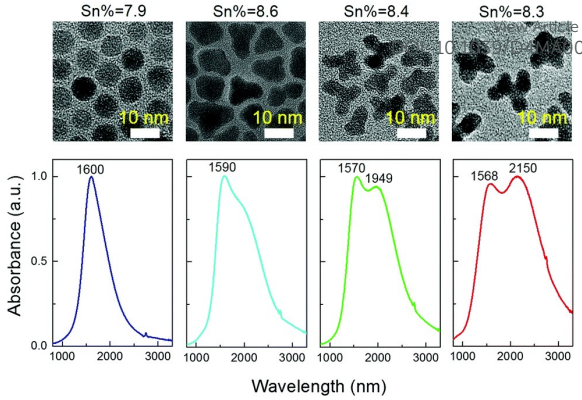

Figure 9 Solution phase UV-Vis-IR absorbance spectra of four shapes (spheres, triangles, tripods and tetrapods) of Sn-doped nanocrystals in CCl_4. The nominal doping concentration is the same (8%) for all of the samples and the real doping concentrations are 7.9%, 8.6%, 8.4%, 8.3%, respectively, determined by ICP-AES techniques. Reproduced from ref. 53 with permission from RSC, copyright 2017.

In_2O_3 Based Nanocrystals

Similarly to its immense use as a transparent conducting oxide (TCO) for devices like solar cell, Sn doped In_2O_3 (ITO) remains the most studied and investigated plasmonic MOXs.[46–49] In fact, degenerately doped In_2O_3 NCs are used as a model to investigate and understand the phenomenon such as defect engineering,[50] dopant distribution,[51] dopant selection[52] etc. In an interesting report Yu Gu et al.[53] have synthesized triangle-, tripod-, and tetrapod-branched ITO NCs with heat-up method for anisotropic infrared plasmonic. Fig. 9 showed the UV-VIS-IR spectra along with the TEM images. Clearly, NCs LSPR characteristics strongly correlated with the shape of NCs. Particularly, beside the spherical ITO NCs, addition component appears at a lower plasmon energy which also intensified and shifts towards lower energy (red shift) with increase in the anisotropy of NCs shape. Conversely, the LSPR peak at high energy is slightly blue shifted. In order to understand the shape dependence of LSPR characteristics, finite-difference time-domain (FDTD) simulation were performed. The detailed analysis showed that the low-energy and high energy peaks are attributed to the in-plane and out-of-plan polarizations. The in-plane polarization is responsible for the excitation of A_2'' mode (triangles and tripods) of the D_{3h} point group and the A_{2u} mode (tetrapods) of the D_{4h} point group. On the other hand, out-of-plane mode related to the E′ mode (triangles and tripods) of the D_{3h} point group and the E_u mode (tetrapods) of the D_{4h} point group. Other than the shape of NCs, the dopant distribution is also found to affect their plasmonic properties.[51] Fig. 10a showed the optical extinction coefficient of ITO NCs at different doping level of Sn and XPS depth profiling of Sn in NCs (fig.10b). Clearly with the doping content up to 5.1%, the gradual increase in peak intensity and blue shift is observed. While, when Sn doping content further increases to 7.6%, redshift is observed, which is an indication of irreducible Sn complexes formation along with the oxygen interstitial atoms. Furthermore, surface Sn content exhibits linear relationship until the Sn doping content of 5.1% (see fig. 10b). This attributed to the uniform distribution of dopant (Sn) in the NCs. While when doping level further increases, the abrupt increase in surface Sn content is

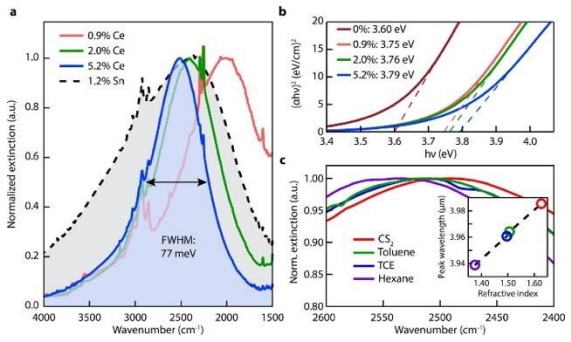

Figure 10 Optical properties of Ce:In_2O_3 nanocrystals. (a) FTIR liquid cell spectra of Ce:In_2O_3 and Sn:In_2O_3 nanocrystals dispersed in tetrachloroethylene showing narrow and tunable MIR LSPR of Ce:In_2O_3. (b) Tauc plot showing systematic increase of Ce:In_2O_3 optical bandgap with Ce content consistent with a Burstein–Moss shift. (c) LSPR of 5.2% Ce-doped In_2O_3 dispersed in nonpolar solvents with different refractive indices. Inset: LSPR peak wavelength versus refractive index. Reproduced from ref. 50 with permission from ACS, copyright 2016.

observed which was for 650 eV photons as compared to 1150 eV photons. This indicated the surface segregation of Sn at higher doping level.

Furthermore, in another interesting work by Milliron et al.[50] cerium (Ce) doped- In_2O_3 based NCs were proposed. To synthesize Ce:In_2O_3 NCs, indium acetylacetonate, cerium precursor, and OLA were mixed in a three-neck round bottom flask, connected to the Schlenk line and heated to 250 °C for 2 h in an inert environment. Fig.11 represents the optical characterization of Ce:In_2O_3 NCs with the different doing content of Ce. As shown in the fig.11a, the Ce:In_2O_3 NCs exhibits narrow LSPR peak as compared to ITO NCs with peak shifted to the higher energy with increase in the Ce content. Furthermore, the band gap of NCs were also found to increase with increase in Ce doping. Further, when NCs dispersion were made in different nonpolar solvents (with increasing refractive index), the redshift in the LSPR peak is observed (see fig. 11c). Additionally, Ce:In_2O_3 NCs were found to exhibit electron mobility value of 33 cm^2V^{-1} s^{-1}, that were higher than ITO NCs, make them ideal of transparent conducting applications. Furthermore, S. H. Cho et a.[54] have synthesized fluorine (F), Sn co-doped In_2O_3 NCs with hot-injection method. The co-doped NCs exhibits LSPR characteristics in the NIR region.

Furthermore, molybdenum (Mo) and tungsten (W) are also incorporated into the In_2O_3 and showed LSPR in mid-IR region.[55] To synthesize Mo and WO NCs doped In_2O_3 NCs (IMO and IWO), the metal/dopant precursors were mixed with OLA and heated at 250 °C and 300°C respectively. Figure 12 showed the LSPR absorption spectra and Tauc plot of IMO and IWO NCs. Clearly, both NCs exhibits LSPR in the mid-IR region with peak shifted to higher energy with increase in doping content of Mo and W. Furthermore, the band-gap is also increase with increase in doping due to the Burstein-Moss effect. Similarly, antimony (Sb) and titanium (Ti) doped In_2O_3 NCs exhibits LSPR in mid-IR region.[56] At the similar doping level of Sb and Ti, the LSPR of Ti-doped NCs was found to be at the lower energies and possessed smaller bandwidths compared to Sb-doped In_2O_3 NCs. This indicates the lower density of free electrons in Ti-doped In_2O_3 NCs. In an impressive work, the first-time synthesis of zirconia

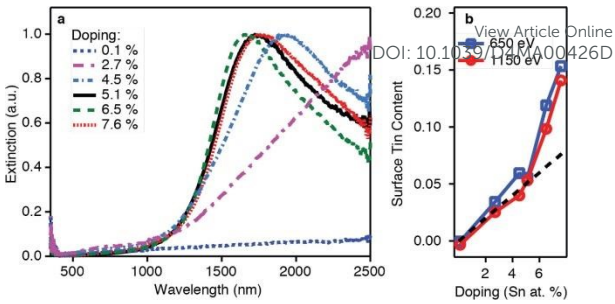

Figure 11(a) Optical extinction and (b) XPS depth profiling versus doping for the doping series. The dotted black line in panel b shows the expected Sn/(In + Sn) ratio for a uniform doping profile. Reproduced from ref. 51 with permission from ACS, copyright 2014.

(Zr) doped In_2O_3 NCs via hot-injection method.[52] By calculating the quality factor (Q-factor) of LSPR, which is defined as the ratio of LSPR peak energy to its line width, author represented the dopant selection criteria. It has been found that for high LSPR energy, a stable oxidation state and deeper donor state in the conduction band of host is required. While for small LSPR full width at half maximum (FWHM) requires the higher charge/radius ratio and lower electronegativity of the dopant cation correspond to the host cation. In this regard, Zr is found to be ideal aliovalent dopant for In_2O_3 as it exhibits highest Q-factor compared to the any other plasmonic material reported in the literature so far. The FTIR spectra of Zr doped-In_2O_3 NCs with different doping content and corresponding Q-value is shown in figure 13. Clearly, NCs showed LSPR fingerprints in mid-IR region.

ZnO Based Nanocrystals

Among all the different MOXs, ZnO remains the centre of interaction after ITO for optoelectronics owing to its large exciton binding energy which is 60meV.[57] In particular AZO

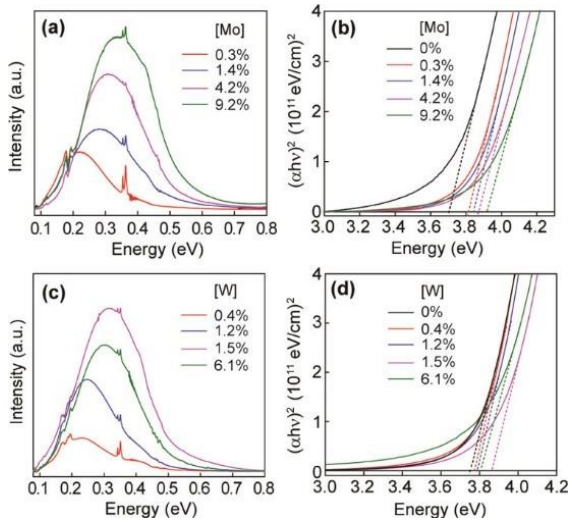

Figure 12(a) LSPR absorption spectra of IMO NCs having different doping concentrations, as indicated in the graph. (b) Tauc plots for IMO NCs from panel (a) used to determine optical band gaps. (c) LSPR absorption spectra of IWO NCs having different doping concentrations, as indicated in the graph. (d) Tauc plots for IWO NCs from panel (c) used to determine optical band gaps. Reproduced from ref. 55 with permission from ACS, copyright 2019.

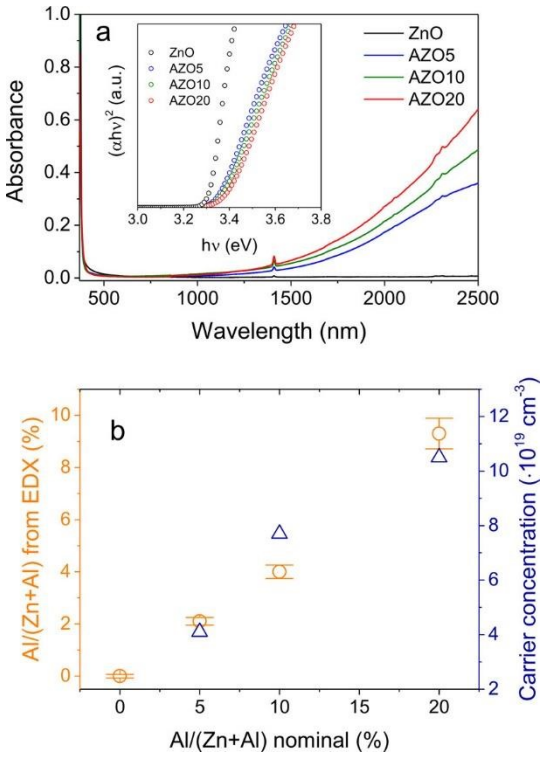

Figure 13 Synthesis of Al-doped ZnO NCs. (a) UV–vis–NIR spectra of ZnO NCs doped with different amounts of Al. The inset shows the respective Tauc plots. (b) Charge carrier concentration evaluated from the LSPR frequency and nominal vs real (from EDX) Al concentration for ZnO NC doped with different amounts of aluminum. Reproduced from ref. 59 with permission from ACS, copyright 2019.

isregarded as a leading candidate for the replacement of ITO as transparent conducting oxide (TCO).[58] Due to its remarkable optoelectronics properties, continuous effort has been made to obtain and tune the LSPR over the wide range of IR region by incorporating different dopants such as Al, In, Ge, Ga etc.

P. Wainer et al.[59] have synthesized Al-doped ZnO NCs with continuous growth methods. In a typical synthesis, first the solution of metal precursor and dopant was prepared in oleic acid (OA) and oleylamine (OLA) which was then slowly injected (3ml/min.) to preheated oleyl alcohol. Fig. 14a showed the UV-VIS-NIR spectra (inset indicates the band gap) of pristine and Al-doped ZnO (AZO) NCs with different dopant percentage (AZO5: 5%Al, AZO10:10%Al and AZO: 20%Al). Clearly, the AZO NCs exhibits LSPR in NIR region whose intensity found to increase with increase in doping concentration. Additionally, the band-gap is also found to increase with dopant concentration due to the Brustein-Moss effect. Furthermore, the carrier concertation up to 10^{20} cm^{-3} was achieved with the highest doping level of aluminium (see fig. 14b). Indeed, author were able to incorporate 40% of Al in ZnO NCs. In another interesting work, ZnO NCs doped with In, Ga and Al were prepared by non-injection method (heat-up).[60] Initially, precursors (metal and dopant), surfactant and solvent are mixed together in nitrogen atmosphere at 100-140 °C and then the temperatures gradually increased up to 250 °C at a rate ~4 °C/min., that leads to the formation of NCs. In the figure 15, surface morphology of ZnO, AZO, Ga-doped ZnO (GZO) and In-doped ZnO (IZO) NCs along with their size distribution were shown. As it can be seen from

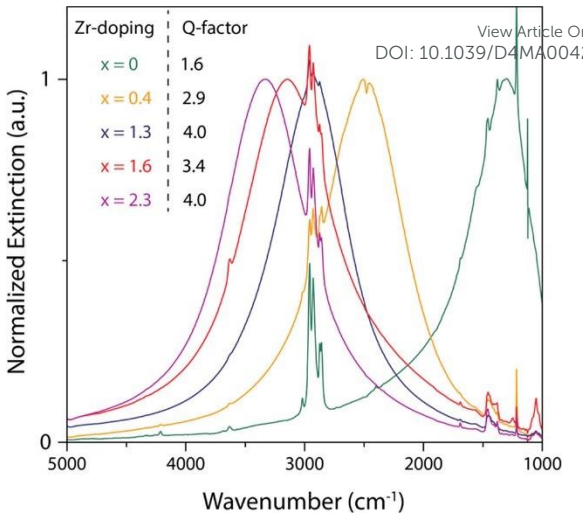

Figure 14 Optical extinction spectra of different Zr:In_2O_3 NCs displaying narrow and symmetric LSPR bands increasing in energy with an increase in Zr doping. Spectra were taken by FTIR of NCs dispersed in tetrachloroethylene. Reproduced from ref. 52 with permission from ACS, copyright 2019.

TEM images, NCs seemed to exhibit both spherical and elongated shapes (few rod-like also). The sizes of ZnO, AZO, GZO and IZO was found to be 11.2 ± 2.1 nm, 27.1 ± 6.0, 17.5 ± 3.1, and 13.4 ± 2.4 nm respectively. Furthermore, optical characterization (UV-VIS-NIR and FTIR) of all the NCs along with a picture of stock solution and their XRD pattern were shown in figure 16. Beside undoped ZnO NCs, all the doped NCs exhibits LSPR in the NIR region. The FTIR study reveals that the LSPR of AZO, GZO, and IZO showed peak value at 7.5, 5, and 3 µm. According to the Drude-Lorentz theory, the frequency of LSPR resonance can be related to the charge-carrier density (n) by following equation:

$$n = \omega^2 m_e e_o (\varepsilon_\infty + 2\varepsilon_m)/e^2$$

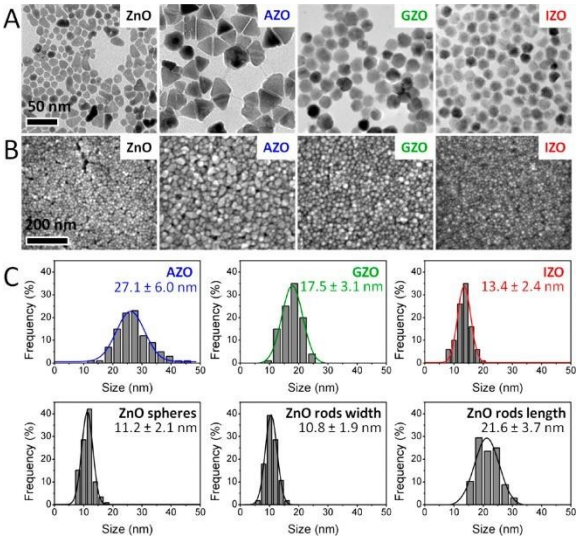

Figure 15 Electron microscopy characterization of ZnO-based NCs. (A) TEM images (the scale bar is the same in all TEM images). (B) SEM images (the scale bar is the same in all SEM images). (C) Histograms of size distribution evaluated from TEM images. Reproduced from ref. 60 with permission from Authors: E. Della Gaspera, and J. J. Jasienia , ACS copyright 2014.

where ω is the resonance angular frequency of LSPR in NCs, m_e is the electron effective mass (9.11×10^{-31}kg), ε_0 is the permittivity of free space (8.854×10^{-12} F m^{-1}), ε_∞ is the high-frequency dielectric constant which is 3.71 for ZnO, ε_m is the dielectric constant of the medium surrounding the NCs e.g. solvent in which NCs are dispersed, and e is the electron charge, 1.6×10^{-19} C. This equation clearly indicates that the LSPR resonance frequency ω is directly proportional to the carrier-concentration n (inversely proportional to wavelength). In the present case, the carrier concentration for AZO, GZO, and IZO NCs were found to be ~4.2×10^{19}, ~9.4×10^{19}, and ~2.6×10^{20} cm^{-3} respectively. Thus, due to the highest carrier concentration in IZO NCs, its LSPR resonance appears at lower wavelength as compared to other doped NCs. Moreover, all the NCs possessed typical wurtzite structure as shown in XRD spectra (fig. 16D). Furthermore, the size and dopant controlled AZO NCs were synthesized by Milliron et al.[9] In this work, the use of coordinating ligands in the synthesis process provides the control over reaction between metal and dopant precursors that in-turn helps to tune the Al doping content in NCs from 0 to 8%. While, changing the growth temperature helps to maintain the size of NCs between 5 and 20 nm. To synthesize AZO NCs, precursor solution containing 1mM zinc stearate ($ZnSt_2$), 0.05-0.5 mM aluminium acetylacetonate ($Al(acac)_3$), 3mL OA in 4mL octadecene (ODE) was injected into the solution of 10ml 1,2-hexadecanediol (HDDIOL) in 11 mL of ODE which was preheated at 230-260 °C. the reaction was performed in argon inert environment. After the addition of precursor solution, the temperature was found to dropped by 20 °C that leads to the formation of narrow sized NCs. While gradual increase in temperature leads to the formation bigger NCs. Fig. 17 showed the TEM images of NCs grown at different temperatures i.e. at 230°C (fig. 17A), 240 °C (fig. 17B) and 260 °C (fig. 17C). Furthermore, all the AZO NCs doped with different Al content exhibits LSPR in the NIR region. With increase in the doping content of Al, the intensity of IR absorption increased monotonically and LSPS resonance shifted to the high energy (towards lower wavelength). In another interesting work, M. Saha et al.[61] have reported the hot-injection synthesis of hexagonal shaped trivalent Ga doped ZnO

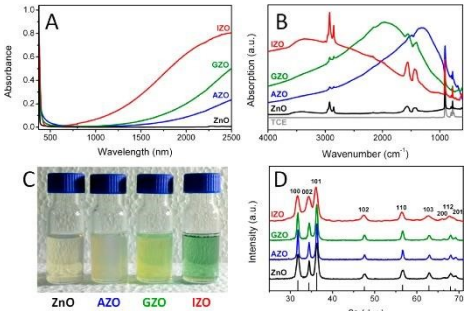

Figure 16 (A) Optical absorption spectra of equimolar solutions of ZnO-based NCs in TCE. (B) FTIR spectra of the same colloidal solutions. (C) Picture of the concentrated stock solutions (absorption spectra are obtained by diluting the stock solutions ~50 times). (D) XRD patterns of the dried powders (the predicted diffraction peaks for bulk wurtzite ZnO are displayed at the bottom). Reproduced from ref. 60 with permission from Authors: E. Della Gaspera, and J. J. Jasienia , ACS copyright 2014.

NCs (GZO). The UV-VIS-NIR and FTIR spectra of GZO NCs are shown in figure 18. As shown in the figure 18a, all GZO NCs exhibits LSPR characteristics in the NIR region and until the doping content of Ga x=0.02, the peak intensity is monotonically increased. However, further increase in doping content x=0.04,

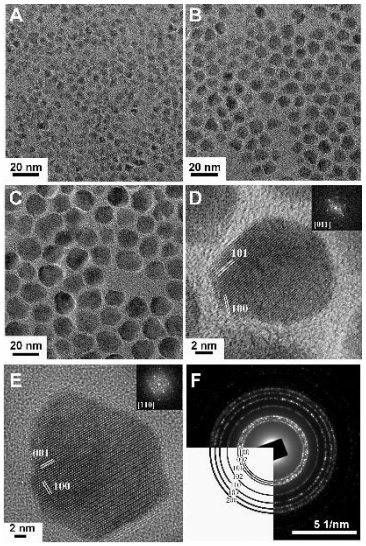

Figure 17 Low- and high-resolution TEM images of AZO NCs. (A–C) AZO NCs of different sizes were obtained by injecting precursor solutions containing 0.2 mmol of $Al(acac)_3$ at 230, 240, and 260 °C, respectively. (D) HRTEM image of a pseudospherical AZO NC oriented along the [011] zone axis and the corresponding fast Fourier transform (FFT) in the inset indicating the hexagonal structure of the wurtzite. The lattice fringes correspond to spacings of 2.42 and 2.79 Å derived from FFT which match well the *d* spacing of the (101) (d_{ZnO}^{101} = 2.47 Å) and (100) planes (d_{ZnO}^{100} = 2.81 Å) of wurtzite ZnO. (E) HRTEM image of a bullet-shaped AZO NC oriented along the [110] zone axis and the corresponding FFT in the inset. The lattice fringes correspond to 2.79 and 2.58 Å, derived from FFT, consistent with the (100) and the (001) (d_{ZnO}^{001}=2.60 Å) planes, respectively, of wurtzite ZnO. (F) Electron diffraction of AZO NCs with the expected wurtzite pattern indicated in the lower left. Reproduced from ref. 9 with permission from ACS, copyright 2011.

a concomitant decrease in the IR absorption is observed. Authors associate this decrease to three possible reasons: *i*. inhomogeneous doping of Ga; *ii*. electron trapping around the Ga^{3+} ion; *iii*. obliteration of NCs size distribution. These results indicate that the doping content must be carefully optimized to obtain strong LSPR characteristics. Furthermore, Gaspera et al.[62] have synthesized the germanium (Ge) doped ZnO colloidal NCs for the very first time by employing heat-up method. In a typical synthesis, the Ge precursor i.e. [Ge(O,O'-glycolate)$_2$(H_2O)$_2$] is dissolved in OLA at 120 °C under cooling. After cooling the Ge precursor solution, it was added in the $ZnSt_2$ solution in mixture of OA, 1-dodecanol and ODE. After the addition, the solution was heated at 230 °C for 2 hours that leads to the formation of Ge-doped ZnO NCs. The UV-VIS-NIR absorption spectra of Ge-Doped ZnO NCs is shown in fig. 19a along with the Tauc plot on fig. 19b. All the doped NCs exhibits LSPR in the NIR region which increase with increase in the doping level of Ge. On the other hand, band gap is also found to increase with increase in doping content which is the indication of Burstein- Moss effect. Figure 19c is representation of band-

View Article Online
DOI: 10.1039/D4MA00426D

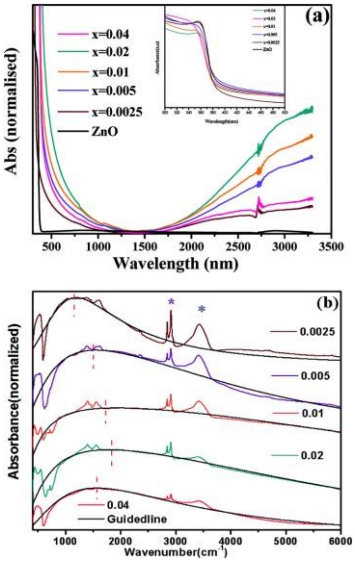

Figure 18(a) Optical absorption spectra of pure ZnO and doped $Zn_{1-x}Ga_xO$ nanocrystals in the VIS-NIR region. The inset depicts band gap absorption of samples. (b) FTIR spectra of doped samples showing the plasmonic NIR absorption. Additional sharp peaks (asterisks) arise from organic ligand oleylamine absorbed on the nanocrystal surface. Blue and purple asterisks represent N–H stretching and symmetric/asymmetric stretching vibration of long hydrocarbon chains, respectively. The black dotted line and the red vertical dotted line are guiding lines for shifting of plasmonic absorption. Reproduced from ref. 61 with permission from RSC, copyright 2015.

gap with increase in the doping level of Ge in ZnO NCs. In a similar work, W. Zhu et al.[63] have investigated the change in the structural and composition caused by Ge doping in ZnO NCs. Again, the ZnO NCs were fabricated using heat-up method and their thin film was deposited by spin coating. The detailed investigation reveals that degenerate doping of ZnO NCs with Ge reduces the intrinsic defects in ZnO and suppresses the emission in the green-red region from defects and free exciton. The suppression of emission was found to be caused by the substitution of Ge^+ at Zn sites and the formation of non-radiative deep-level traps $(GeZn)^+$.

WO_{3-x} Based Nanocrystals

The reduced form of WO_3 i.e. WO_{3-x} exhibits strong LSPR features in the NIR region,[64–68] owing to the presence of oxygen vacancies in crystal lattice.[69] The WO_{3-x} possessed strong blue and can be obtained in variety of stoichiometry i.e. $WO_{2.83}$ ($W_{24}O_{68}$), $WO_{2.72}$ ($W_{18}O_{49}$), $WO_{2.8}$ (W_5O_{14}) and $WO_{2.9}$ ($W_{20}O_{58}$). [15] K. Manthiram et al.[15] have synthesized nanorods shaped $WO_{2.83}$ NCs via hot-injection method with tuneable LSPR. Fig. 20 showed the UV-ViS-NIR spectra of $WO_{2.83}$ nanorods suspension in N-methylpyrollidone (fig.20a), along with its crystalline properties(fig.20b). Particularly in fig. 20b, the LSPR features of $WO_{2.83}$ nanorods heated at 175 °C for 0, 2 and 6 minutes are presented. Clearly upon heating, the intensity of LSPR peak is decreased and peak is shifted to higher wavelength (red shift) which is due to the decrease in carrier concentration caused by the oxidation of $WO_{2.83}$. On the other hand, the absorption edge exhibits blue shift upon heating. Furthermore, decrease in the crystallinity of nanorods is observed when heated at 175 °C for 6 minutes. In another work, cesium doped tungsten oxide

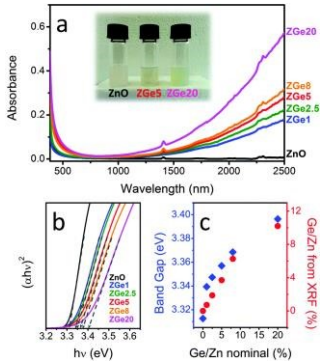

Figure 19 (a) Optical absorption spectra of equimolar colloidal solutions of ZnO:Ge in tetrachloroethylene (TCE). The inset shows a digital picture of the prepared colloidal solutions. (b) Tauc plot (exponent = 2, direct band gap) of the ZnO:Ge colloidal solutions. The dashed lines are the linear fits used to identify the band gap. (c) Optical band gap and real Ge/Zn amount evaluated from XRF as a function of the nominal Ge/Zn ratio. Reproduced from ref. 62 with permission from RSC, copyright 2015.

(Cs_xWO_3) NCs were prepared and explored to evaluate their plasmonic properties.[69] These types of interstitially doped tungsten oxide are also known as tungsten bronze with formula M_xWO_3 (M: Li^+, Na_+, Cs^+, or Rb^+). The NCs were prepared by Fig. 21 showed the TEM images of pristine $WO_{2.72}$ nanorods and Cs_xWO_3 NCs in three different shapes: hexagonal prism, truncated cube, and pseudospheres. These doped NCs exhibits LSPR in the NIR region. Furthermore, WO_{3-x} NCs prepared by solvothermal methods showed string plasmonic behaviour in the Vis-NIR region.[70] Fig. 22 showed the UV-ViS-NIR absorbance spectra of WO_{3-x} NCs in protic polar solvents. In the cased of NCs dispersed in ethanol, extremely well resolved plasmonic peak at 556nm were observed.

CdO Based NCs

Cadmium Oxide (CdO) is another n-type wide-band gap MOXs that showed LSPR with[71,72] or without doping[73]. Fig. 23 showed the TEM images of octahedral shaped In-doped CdO (ICO) NCs along with the pictorial representation of ICO unit cell.[71] This

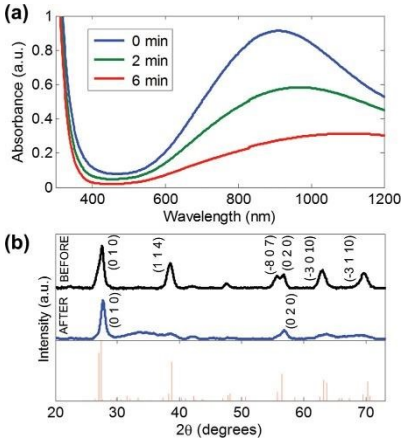

Figure 20 (a) UV–vis–NIR absorption spectra of $WO_{2.83}$ nanorods in *N*-methylpyrrolidone upon heating at 175 °C in air for 0, 2, and 6 min. (b) XRD patterns of $WO_{2.83}$ nanorods in *N*-methylpyrrolidone (top) before and (middle) after heating at 175 °C for 6 min in air and (bottom) the reference pattern for $WO_{2.83}$. Reproduced from ref. 15 with permission from ACS, copyright 2012.

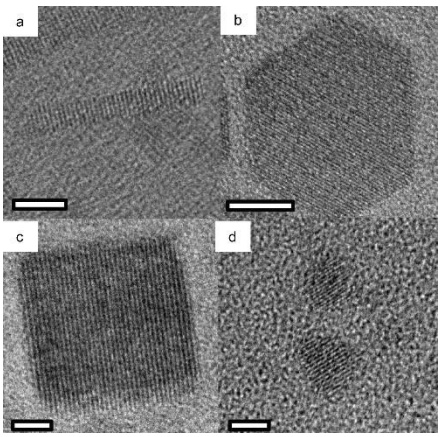

Figure 21 High-resolution TEM images of (a) $WO_{2.72}$ rods and Cs_xWO_3 (b) hexagonal prism, (c) truncated cube, and (d) pseudospheres. All scale bars are 5 nm. Reproduced from ref. 69 with permission from ACS, copyright 2014.

was the first report on ICO NCs synthesized using heat-up method in both spherical and octahedral shape. As it can be seen from fig. 23, compatibly larger ICO NCs were formed when oleic acid (OA) concentration was 3 mM. Furthermore, the absorption spectra indicating the LSPR feature of ICO NCs (from NIR to MIR) and band-gap at different doping content of In (see fig. 24). With increase in In-doping content the LSPR peak is blue shifter. Additionally, as expected, the band gap is also increased with doping content. On the other hand, undoped CdO NCs whose LSPR was tuned from the wide-range of NIR to MIR region was synthesized via decomposition of cadmium acetylacetonate ($Cd(acac)_2$) at 316 °C.[73] In order to promote the oxygen deficiency, reducing agents such bis(trimethylsilyl)amine (HMDS) is introduced in reaction mixture. The idea behind using reducing agent is to control the free electron concentration that will in-turn affect the LSPR positioning. It has been found that by increasing the HMDS/Cd molar ratio, the NCs diameter decreases monotonically from 44.9 to 5.2 nm. Figure 25a showed FTIR spectra of CdO NCs with different diameters. Evidently, as diameter of NCs decrease (increase in oxygen deficiency), the LSPR peak shifted toward

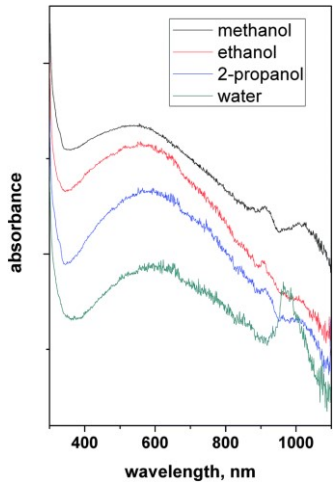

Figure 22 UV-vis-NIR absorbance of WO_{3-x} nanocrystals – LSPRs in different protic polar solvents. Reproduced from ref. 70 with permission from RSC, copyright 2016.

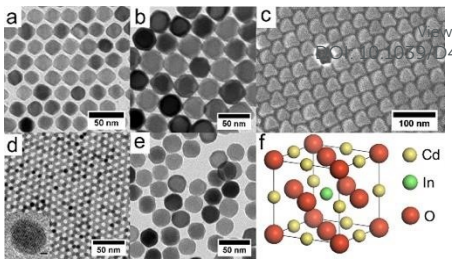

Figure 23 TEM images of octahedral ICO nanocrystals produced at 300 °C using (a) 4 mmol and (b) 3 mmol OLAC and (c) SEM image of sample shown in b. TEM image of spherical nanocrystals produced at reflux using (d) 5 mmol and (e) 3 mmol OLAC. (f) The unit cell of rock-salt type indium-doped cadmium oxide (ICO). Influence of Shape on the Surface Plasmon Resonance of Tungsten Bronze Nanocrystals. Reproduced from ref. 71 with permission from ACS, copyright 2013.

the NIR region. Furthermore, in fig. 25b, the extinction coefficient of NCs dispersed in three different solvents i.e. carbon tetrachloride (CCl_4), tetrachloroethylene (TCE), carbon disulfide (CS_2). As expected, the LSPR peak is shifter to the higher wavelength (red shift) as the refractive index of the solvent increase (see fig. 25c).

Furthermore, fluorine, in codoped CdO (FICO) NCs were syntehsized via heat-up method.[74] Fig. 26 (a,b and c) showed the TEM image, UV-ViS-NIR spectra and Tauc plot of FICO NCs. As seen from Fig.26a, the FICO NCs are found to be spherical in shape. At all the doping concentrations, sharp LSPR peaks were observed which shifted to lower wavelength as doping concentration is increased (fig. 26b). Furthermore, the band gap of FICO NCs was also increased with increase in in doping level underlying the Burstein-Moss effect.

Future Perspective Application: MOXs NCs Based IR photodetector and PV Self-Powered Chemical Sensors

After comprehensive review of literature about the plasmonic properties of different MOXs NCs, we come to their future perspective applications in optoelectronics devices. The first obvious applications of these materials are for IR photodetectors owing to tuneable LSPR in IR region. The continuous increase of interest in (IR) photodetectors have

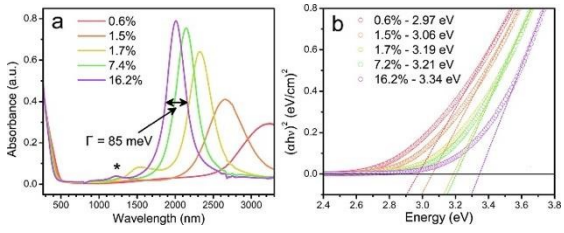

Figure 24 (a) Solution phase spectra of ICO nanocrystals dispersed in CCl_4 for five levels of % atomic doping of In. The fwhm or Γ is indicated for the 16.2% doped sample. (b) Plots of $(\alpha h\nu)^2$ vs photon energy (eV) for five samples of spherical ICO nanocrystals. Open circles are measured data, dotted lines are linear fits, and the legend shows the extracted direct bandgap energies. Reproduced from ref. 71 with permission from ACS, copyright 2013.

View Article Online
DOI: 10.1039/D4MA00426D

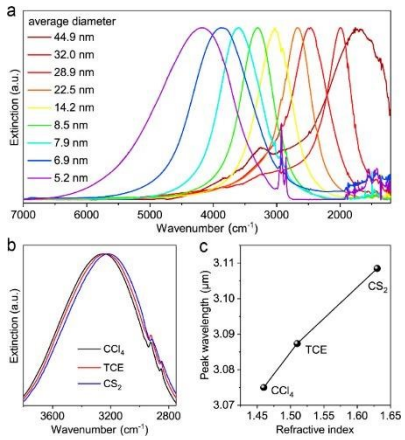

Figure 25 (a) Normalized extinction spectra of size controlled CdO NCs synthesized with different HMDS/Cd ratios. (b) Extinction spectra of CdO NCs (8.5 ± 1.2 nm) dispersed in different solvents. (c) Plot of LSPR peak wavelength versus the refractive index of solvent. CCl_4: carbon tetrachloride, TCE: tetrachloroethylene, CS_2: carbon disulfide. Reproduced from ref. 73 with permission from ACS, copyright 2020.

driven advancements in imaging, satellite remote sensing, environmental monitoring, optical communications, security surveillance, gas identification, and biomedical engineering.[75,76] However, the current commercial IR photodetectors are developed using bulk compound semiconductors like InSb, Ge, HgCdTe, and InGaAs, still grapple with big issues such as high cost, toxicity, inflexibility, low environmental stability, complex fabrication processes, volume-dependent thermal noise, and limited pixel size.[75,77,78] Due to this, continuous effort has been made to find alternative low-cost and highly efficient materials for IR photodetector applications. In this regard, 2D materials (graphene, MXene, TMDs etc.) [22,75,79,79,80] and narrow band gap materials such as PbS,[81] PbSe,[82] InP[83] were put forward. However, 2D materials are still suffered from issues like i) limited availability of 2D materials with bandgap ii) lack of reproducibility in the fabrication process, iii) poor stability under ambient environment iv) slow/poor response dynamics, and v) poor selectivity and vi) large scale rpoduction.[22,75,84–86] . Additionally, the large-scale production of 2D materials is a common challenge faced by both applications.[22,75] On the other hand, narrow-band gap materials based IR photodetectors face several critical challenges discussed by Z. Wang et al.[76] in a comprehensive review article. Particularly, the issues are the use of heavy toxic materials (eg. Pb, Hg) and their better performance mainly in NIR region[81,87,88], while the development of MIR-based photodetectors remains a challenging task. Additionally, these QDs-based IR photodetectors suffer from the poor charge carrier transport in QDs[76] which is a huge problem as the effective charge carrier transport in photodetectors determines the charge carrier separation and collection.

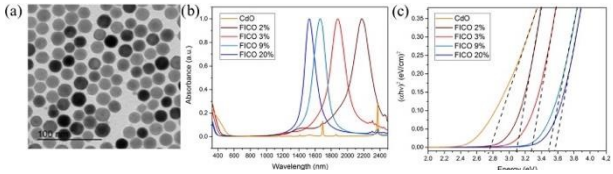

Figure 26 (a) Transmission electron microscopy images of FICO 3% (diameter 20.2 ± 1.8 nm), respectively. (b) Normalized absorption spectra of FICO NCs samples with different doping levels. (c) Plots of $(\alpha h\nu)^2$ vs photon energy ($h\nu$) for the FICO NC samples shown in (b). Reproduced from ref. 74 with permission from ACS, copyright 2019.

Degenerately doped MOXs NCs can be seen as an IR detecting media because of the possibility to tune the LSPR from deep MIR to NIR region via optimizing the carrier concentration using different dopants. Furthermore, the availability of scalable synthesis method like heat-up and continuous growth makes it favourable over 2D materials. In an interesting work, Qu et al.[89] have explored the potential of ITO NCs for IR photodetector applications. Due to the weak photo-signal that linked with the poor charge transport in NCs (similar issue as narrow band gap QDs) and weak extraction of LSPR assisted hot-electrons, very poor photodetector performance was observed. To overcome the obstacle of hot-electrons extraction, the heterostructure of MOXs NCs (ITO) and MoS_2 has recently been proposed, which we have already discussed in section 3. However, while making optoelectronic devices like photodetector, charge transport within the active material and their collection at the respective electrodes defines the efficiency of devices. In this regard, the heterojunction between narrow-band gap PbS QDs and ZnO nanowires (NWs) were proven to be effective,[81,87] in which the QDs act as a NIR sensitizer and NWs provide the condition path to electrons. Indeed, the charge transport in NWs is believed to occur at speed several orders of magnitude faster than nanoparticles like QDs or NCs, primarily attributed to the minimized scattering effects resulting from the limited presence of grain boundaries.[90] Additionally, due to the quantum confinement effect, NWs provide unidirectional and better control of charge transport that leads to high charge-carrier mobility.[90] Hence, the heterojunction of NCs with 2D materials, nanowires etc. can been seen as step forward to fabricate the future generation IR photodetectors based of degenerately doped MOXs NCs.

Furthermore, nanostructured MOXs have been explored and proves to be highly efficient of chemical sensing applications.[91–98] However, recently, the development of self-powered sensors for real-time environmental and health monitoring has gained momentum, driven by the urgency of the energy crisis, environmental pollution, and climate change.[23] Harnessing energy from sunlight is always an ideal and dependable choice due to its cleanliness, safety, and the vast energy reserves Earth receives from sun. The sensor that harnesses energy from sunlight is known as photovoltaic (PV) self-powered sensor.[79] However, the current state-of-art for PV self-powered sensors, whether utilizing sunlight or other activation sources, still far from reaching the essential "3S of sensor": sensitivity, selectivity, and stability.[22,23,99] In this regard, photoactivated (UV) MOX-based gas sensors have gathered significant attention to developing RT or low-power-consuming sensors.[22] By fabricating these MOXs in different nanostructure forms and via tuning their band-gap, photoactivation with visible light has also been achieved.[23] It was observed that via designing suitable device structures these photoactivated MOXs sensors able to achieve self-sustain operation using the photovoltaic (PV) effect.[100–102] To further extend the light harvesting to IR region, degenerately doped MOXs NCs can be employed as an active

DOI: 10.1039/D4MA00426D

sensing platform. Sturaro et al.[103] have proposed the gallium-doped zinc oxide (GZO) NCs based optical (plasmonic) and chemiresistive sensors for the detection of hydrogen (H_2) and nitrogen dioxide (NO_2). To realize the sensing device, the NCs thin film was deposited by spin coating onto SiO_2 substrate. The sensing measurement were performed at 80 and 200 °C. In the chemoresistive gas sensing of these NCs, author have observed some response at room-temperature under the illumination of blue light and the response was increased with increase in the operating temperature of sensor. These were the preliminary investigation as many important factors such as sensor selectivity, sensitivity and stability need to be explored. However, it indeed gives us the idea and possibility to used degenerately doped MOXs NCs to build the PV self-powered sensors that harvest energy form UV-VIS-IR radiation. In this sense, the heterostructure of NCs with MOXs NWs can be effective. These reason behind this argument is that the chemoresistive sensor based on MOXs NWs already an established sensing platform and showed fast response dynamics, selectivity, and stability due to their high surface-to-volume ratio, well-defined crystal orientation and controlled unidirectional electrical properties.[94,104,105]

Hence, by carefully manipulating the plasmonic properties of degenerately doped MOXs NCs and using suitable device configuration, future generation IR photodetectors and PV self-powered chemical sensors can be developed.

Conclusion

In conclusion, via reviewing comprehensive literature, we have demonstrated the plasmonic properties of degenerately doped MOXs NCs. As compared to well-known hot injection method, continuous growth and heat-up represents the large-scale production methods and were used significantly to produce various MOXs NCs. Fabrication of 0D-2D heterostructure (ITO/MoS_2) for the extraction of LSPR-assisted hot-carriers is an interesting strategy. These types of strategies should also be utilized for other MOXs NCs and ultrafast transient absorption studies needed to be done to develop the deep understanding about plasmonic charge-carrier dynamics in MOXs NCs. In fact, after reviewing the literature, we have realized that advanced level of understanding in term of synthesis such as growth mechanism of NCs, incorporation different dopants inside NCs and their effect on LSPR, roles of defects and tuning the LSPR over wide range of IR region via controlling the NCs size and doping content, have already been achieved. Now it's the time to carry out studies at device level such as acquiring IV characteristics under the illumination of IR light and understanding the mechanism of photogenerated charge carriers in a different device configuration such as heterojunctions, thin films of NCs, self-assembly etc. These types of studies are highly important for the practical and perspective use of MOXs NCs for future generation optoelectronic devices. Thus, we believe degenerately doped MOXs NCs have great potential to develop IR photodetectors, PV self-powered sensors and other potential optoelectronics devices, but immense amount of dedicated work is required on a device level.

Author Contributions

MS conceptualized and wrote the original draft of review. **GMP** conceptualized and edited the manuscript. **FS** edited the manuscript and arranged the funding.

Conflicts of interest

There are no conflicts to declare.

Acknowledgements

This project has received funding from the European Research Council (ERC) under the European Union's Horizon 2020 research and innovation program (grant agreement No. [816313]) and under Horizon Europe (grant agreements No. [101061820]). GMP receives funding from the European Union (ERC, EOS, 101115925). Views and opinions expressed are however those of the author(s) only and do not necessarily reflect those of the European Union or the European Research Council. Neither the European Union nor the granting authority can be held responsible for them. This author also acknowledges financial support by the European Union's NextGenerationEU Programme with the IPHOQS Infrastructure [IR0000016, ID D2B8D520, CUP B53C22001750006] "Integrated Infrastructure Initiative in Photonic and Quantum Sciences".

References

1 J. A. Faucheaux, A. L. D. Stanton and P. K. Jain, *J. Phys. Chem. Lett.*, 2014, **5**, 976–985.
2 A. Agrawal, S. H. Cho, O. Zandi, S. Ghosh, R. W. Johns and D. J. Milliron, *Chem. Rev.*, 2018, **118**, 3121–3207.
3 M. Yao, P. Shen, Y. Liu, B. Chen, W. Guo, S. Ruan and L. Shen, *ACS Appl. Mater. Interfaces*, 2016, **8**, 6183–6189.
4 F. Xu, H.-F. Lv, S.-Y. Wu and H.-P. HO, *Sensors Actuators B Chem.*, 2018, **259**, 709–716.
5 R. Bakhtiar, *J. Chem. Educ.*, 2013, **90**, 203–209.
6 X. Gu, T. Qiu, W. Zhang and P. K. Chu, *Nanoscale Res. Lett.*, 2011, **6**, 199.
7 L. Moscardi, G. M. Paternò, A. Chiasera, R. Sorrentino, F. Marangi, I. Kriegel, G. Lanzani and F. Scotognella, *J. Mater. Chem. C*, 2020, **8**, 13019–13024.
8 G. M. Paternò, C. Iseppon, A. D'Altri, C. Fasanotti, G. Merati, M. Randi, A. Desii, E. A. A. Pogna, D. Viola, G. Cerullo, F. Scotognella and I. Kriegel, *Sci. Rep.*, 2018, **8**, 3517.
9 R. Buonsanti, A. Llordes, S. Aloni, B. A. Helms and D. J. Milliron, *Nano Lett.*, 2011, **11**, 4706–4710.
10 S. D. Lounis, E. L. Runnerstrom, A. Llordés and D. J. Milliron, *J. Phys. Chem. Lett.*, 2014, **5**, 1564–1574.
11 J. M. Luther, P. K. Jain, T. Ewers and A. P. Alivisatos, *Nat. Mater.*, 2011, **10**, 361–366.

12 P. Yin, Y. Tan, H. Fang, M. Hegde and P. V Radovanovic, *Nat. Nanotechnol.*, 2018, **13**, 463–467.

13 J. Q. Grim, L. Manna and I. Moreels, *Chem. Soc. Rev.*, 2015, **44**, 5897–5914.

14 X. Liu and M. T. Swihart, *Chem. Soc. Rev.*, 2014, **43**, 3908–3920.

15 K. Manthiram and A. P. Alivisatos, *J. Am. Chem. Soc.*, 2012, **134**, 3995–3998.

16 J. Shi, J. Zhang, L. Yang, M. Qu, D.-C. Qi and K. H. L. Zhang, *Adv. Mater.*, 2021, **33**, 2006230.

17 O. Bierwagen, *Semicond. Sci. Technol.*, 2015, **30**, 24001.

18 S. Wahyuningsih, I. Kartini, A. H. Ramelan, L. N. M. Z. Saputri and H. Munawaroh, *IOP Conf. Ser. Earth Environ. Sci.*, 2017, **75**, 12003.

19 M. Patel, H.-S. Kim and J. Kim, *Adv. Electron. Mater.*, 2015, **1**, 1500232.

20 Z. Ma, J. Zhang, H. Lyu, X. Ping, L. Pan and Y. Shi, in *Metal Oxides*, eds. S. Sagadevan, J. Podder and F. B. T.-M. O. for O. and O.-B. M. A. Mohammad, Elsevier, 2022, pp. 117–150.

21 L. Li, C. X. Shan, B. H. Li, B. Yao, D. Z. Shen, B. Chu and Y. M. Lu, *J. Electron. Mater.*, 2010, **39**, 2467–2470.

22 R. Kumar, X. Liu, J. Zhang and M. Kumar, *Nano-Micro Lett.*, 2020, **12**, 164.

23 X.-L. Liu, Y. Zhao, W.-J. Wang, S.-X. Ma, X.-J. Ning, L. Zhao and J. Zhuang, *IEEE Sens. J.*, 2021, **21**, 5628–5644.

24 Q. Geng, Z. He, X. Chen, W. Dai and X. Wang, *Sensors Actuators B Chem.*, 2013, **188**, 293–297.

25 J.-H. Lin, Y.-J. Chen, H.-Y. Lin and W.-F. Hsieh, *J. Appl. Phys.*, 2005, **97**, 33526.

26 D. C. Dai, S. J. Xu, S. L. Shi, M. H. Xie and C. M. Che, *Opt. Lett.*, 2005, **30**, 3377–3379.

27 J. E. Kuszynski, C. J. Fabiano, E. T. Nguyen, K. Mao, A. K. Ahuja, R. D. Schaller and G. F. Strouse, *J. Phys. Chem. C*, 2023, **127**, 22654–22661.

28 A. Devizis, V. Vaicikauskas and V. Gulbinas, *Appl. Opt.*, 2006, **45**, 2535–2539.

29 X. Zhang, C. Huang, M. Wang, P. Huang, X. He and Z. Wei, *Sci. Rep.*, 2018, **8**, 10499.

30 C. Trovatello, F. Katsch, N. J. Borys, M. Selig, K. Yao, R. Borrego-Varillas, F. Scotognella, I. Kriegel, A. Yan, A. Zettl, P. J. Schuck, A. Knorr, G. Cerullo and S. D. Conte, *Nat. Commun.*, 2020, **11**, 5277.

31 G. Grancini, M. Maiuri, D. Fazzi, A. Petrozza, H.-J. Egelhaaf, D. Brida, G. Cerullo and G. Lanzani, *Nat. Mater.*, 2013, **12**, 29–33.

32 M. Maiuri, M. Garavelli and G. Cerullo, *J. Am. Chem. Soc.*, 2020, **142**, 3–15.

33 N. Kinsey, C. DeVault, J. Kim, M. Ferrera, V. M. Shalaev and A. Boltasseva, *Optica*, 2015, **2**, 616–622.

34 G. X. Ni, L. Wang, M. D. Goldflam, M. Wagner, Z. Fei, A. S. McLeod, M. K. Liu, F. Keilmann, B. Özyilmaz, A. H. Castro Neto, J. Hone, M. M. Fogler and D. N. Basov, *Nat. Photonics*, 2016, **10**, 244–247.

35 P. Guo, R. D. Schaller, J. B. Ketterson and R. P. H. Chang, *Nat. Photonics*, 2016, **10**, 267–273.

36 I. Kriegel, C. Urso, D. Viola, L. De Trizio, F. Scotognella, G. Cerullo and L. Manna, *J. Phys. Chem. Lett.*, 2016, **7**, 3873–3881.

37 Q. Guo, Z. Qin, Z. Wang, Y.-X. Weng, X. Liu, G. Xie and J. Qiu, *ACS Nano*, 2018, **12**, 12770–12777.

38 C. Lee, Y. Park and J. Y. Park, *RSC Adv.*, 2019, **9**, 18371–18376.

39 M. Guizzardi, M. Ghini, A. Villa, L. Rebecchi, Q. Li, G. Mancini, F. Marangi, A. M. Ross, X. Zhu, I. Kriegel and F. Scotognella, *J. Phys. Chem. Lett.*, 2022, **13**, 9903–9909.

40 V. K. LaMer and R. H. Dinegar, *J. Am. Chem. Soc.*, 1950, **72**, 4847–4854.

41 C. B. Murray, D. J. Norris and M. G. Bawendi, *J. Am. Chem. Soc.*, 1993, **115**, 8706–8715.

42 S. Ghosh, M. Saha and S. K. De, *Nanoscale*, 2014, **6**, 7039–7051.

43 T. Hyeon, S. S. Lee, J. Park, Y. Chung and H. Bin Na, *J. Am. Chem. Soc.*, 2001, **123**, 12798–12801.

44 B. H. Kim, W. Ko, J. H. Kim, J. S. Georgiou, M. S. Bootharaju, J. Park and T. Hyeon, *Isr. J. Chem.*, 2023, **n/a**, e202200103.

45 A. W. Jansons, K. M. Koskela, B. M. Crockett and J. E. Hutchison, *Chem. Mater.*, 2017, **29**, 8167–8176.

46 B. M. Crockett, A. W. Jansons, K. M. Koskela, D. W. Johnson and J. E. Hutchison, *ACS Nano*, 2017, **11**, 7719–7728.

47 M. Xi and B. M. Reinhard, *J. Phys. Chem. C*, 2018, **122**, 5698–5704.

48 A. M. Schimpf, S. D. Lounis, E. L. Runnerstrom, D. J. Milliron and D. R. Gamelin, *J. Am. Chem. Soc.*, 2015, **137**, 518–524.

49 M. A. Blemker, S. L. Gibbs, E. K. Raulerson, D. J. Milliron and S. T. Roberts, *ACS Photonics*, 2020, **7**, 1188–1196.

50 E. L. Runnerstrom, A. Bergerud, A. Agrawal, R. W. Johns, C. J. Dahlman, A. Singh, S. M. Selbach and D. J. Milliron, *Nano Lett.*, 2016, **16**, 3390–3398.

51 S. D. Lounis, E. L. Runnerstrom, A. Bergerud, D. Nordlund and D. J. Milliron, *J. Am. Chem. Soc.*, 2014, **136**, 7110–7116.

52 B. Tandon, S. Ghosh and D. J. Milliron, *Chem. Mater.*, 2019, **31**, 7752–7760.

53 Y. Gu, Z. Zhu, J. Song and H. Zeng, *Nanoscale*, 2017, **9**, 19374–19383.

54 S. H. Cho, K. M. Roccapriore, C. K. Dass, S. Ghosh, J. Choi, J. Noh, L. C. Reimnitz, S. Heo, K. Kim, K. Xie, B. A. Korgel, X. Li, J. R. Hendrickson, J. A. Hachtel and D. J. Milliron, *J. Chem. Phys.*, 2020, **152**, 14709.

55 P. Yin, Y. Tan, M. J. Ward, M. Hegde and P. V Radovanovic, *J. Phys. Chem. C*, 2019, **123**, 29829–29837.

56 H. Fang, M. Hegde, P. Yin and P. V Radovanovic, *Chem. Mater.*, 2017, **29**, 4970–4979.

57 S. Fiedler, L. O. L. C. Lem, C. Ton-That, M. Schleuning, A. Hoffmann and M. R. Phillips, *Sci. Rep.*, 2020, **10**, 2553.

58 M. Singh and F. Scotognella, *Micromachines*, 2023, 14.

59 P. Wainer, O. Kendall, A. Lamb, S. J. Barrow, A. Tricoli, D. E. Gómez, J. van Embden and E. Della Gaspera, *Chem. Mater.*, 2019, **31**, 9604–9613.

60 E. Della Gaspera, A. S. R. Chesman, J. van Embden and J. J. Jasieniak, *ACS Nano*, 2014, **8**, 9154–9163.

61 M. Saha, S. Ghosh, V. D. Ashok and S. K. De, *Phys. Chem. Chem. Phys.*, 2015, **17**, 16067–16079.

62 E. Della Gaspera, N. W. Duffy, J. van Embden, L.

Waddington, L. Bourgeois, J. J. Jasieniak and A. S. R. Chesman, *Chem. Commun.*, 2015, **51**, 12369–12372.
63 W. Zhu, T. Kammuri, S. Kitamura, M. Sturaro, A. Martucci and G. Pezzotti, *J. Phys. D. Appl. Phys.*, 2018, **51**, 85302.
64 J. T. Lee, S. Hati, M. M. Fahey, J. M. Zaleski and R. Sardar, *Chem. Mater.*, 2022, **34**, 3053–3066.
65 Y.-Y. Li, C.-Y. Zhong, M.-X. Li, Q.-Y. Zhang, Y. Chen, Z.-Q. Liu and J. Z. Zhang, *J. Mater. Chem. C*, 2021, **9**, 1614–1621.
66 J. Chen, Y. Ren, T. Hu, T. Xu and Q. Xu, *Appl. Surf. Sci.*, 2019, **465**, 517–525.
67 T. Masuda and H. Yao, *J. Phys. Chem. C*, 2020, **124**, 15460–15467.
68 P. Li, L. Zhu, C. Ma, L. Zhang, L. Guo, Y. Liu, H. Ma and B. Zhao, *ACS Appl. Mater. Interfaces*, 2020, **12**, 19153–19160.
69 T. M. Mattox, A. Bergerud, A. Agrawal and D. J. Milliron, *Chem. Mater.*, 2014, **26**, 1779–1784.
70 O. A. Balitskii, D. Moszyński and Z. Abbas, *RSC Adv.*, 2016, **6**, 59050–59054.
71 T. R. Gordon, T. Paik, D. R. Klein, G. V Naik, H. Caglayan, A. Boltasseva and C. B. Murray, *Nano Lett.*, 2013, **13**, 2857–2863.
72 S. Ghosh, M. Saha, S. Paul and S. K. De, *Small*, 2017, **13**, 1602469.
73 Z. Liu, Y. Zhong, I. Shafei, S. Jeong, L. Wang, H. T. Nguyen, C.-J. Sun, T. Li, J. Chen, L. Chen, Y. Losovyj, X. Gao, W. Ma and X. Ye, *Nano Lett.*, 2020, **20**, 2821–2828.
74 R. Giannuzzi, F. De Donato, L. De Trizio, A. G. Monteduro, G. Maruccio, R. Scarfiello, A. Qualtieri and L. Manna, *ACS Appl. Mater. Interfaces*, 2019, **11**, 39921–39929.
75 J. Zha, M. Luo, M. Ye, T. Ahmed, X. Yu, D.-H. Lien, Q. He, D. Lei, J. C. Ho, J. Bullock, K. B. Crozier and C. Tan, *Adv. Funct. Mater.*, 2022, **32**, 2111970.
76 Z. Wang, Y. Gu, X. Li, Y. Liu, F. Liu and W. Wu, *Adv. Opt. Mater.*, 2023, **11**, 2300970.
77 M. Long, Y. Wang, P. Wang, X. Zhou, H. Xia, C. Luo, S. Huang, G. Zhang, H. Yan, Z. Fan, X. Wu, X. Chen, W. Lu and W. Hu, *ACS Nano*, 2019, **13**, 2511–2519.
78 L. Ye, H. Li, Z. Chen and J. Xu, *ACS Photonics*, 2016, **3**, 692–699.
79 Y. Niu, J. Zeng, X. Liu, J. Li, Q. Wang, H. Li, N. F. de Rooij, Y. Wang and G. Zhou, *Adv. Sci.*, 2021, **8**, 2100472.
80 S. Gasso and A. Mahajan, *ACS Appl. Nano Mater.*, 2023, **6**, 6678–6692.
81 H. Zhong, L. Tang, P. Tian, L. Yu, W. Zuo and K. S. Teng, *Sensors*, 2023, 23.
82 Y. Shi, Z. Wu, X. Dong, P. Chen, J. Wang, J. Yang, Z. Xiang, M. Shen, Y. Zhuang, J. Gou, J. Wang and Y. Jiang, *Nanoscale*, 2021, **13**, 12306–12313.
83 G. Almeida, R. F. Ubbink, M. Stam, I. du Fossé and A. J. Houtepen, *Nat. Rev. Mater.*, 2023, **8**, 742–758.
84 M. Malik, M. A. Iqbal, J. R. Choi and P. V Pham, *Front. Chem.* , 2022, 10.
85 K. Zhang, L. Zhang, L. Han, L. Wang, Z. Chen, H. Xing and X. Chen, *Nano Express*, 2021, **2**, 12001.
86 E. Lee and H. Yoo, *Molecules*, 2021, 26.
87 H. Wang, T. Kubo, J. Nakazaki, T. Kinoshita and H. Segawa, *J. Phys. Chem. Lett.*, 2013, **4**, 2455–2460.
88 J. Wang and J. Chen, *Surfaces and Interfaces*, 2022, **30**, 101945.
89 J. Qu, C. Livache, B. Martinez, C. Gréboval, A. Chu, E. Meriggio, J. Ramade, H. Cruguel, X. Z. Xu, A. Proust, F. Volatron, G. Cabailh, N. Goubet and E. Lhuillier, *ACS Appl. Nano Mater.*, 2019, **2**, 1621–1630.
90 F. Mei, D. Sun, S. Mei, J. Feng, Y. Zhou, J. Xu and X. Xiao, *Adv. Phys. X*, 2019, **4**, 1592709.
91 M. Singh, N. Kaur, A. Casotto, L. Sangaletti, N. Poli and E. Comini, *J. Mater. Chem. A*, 2022, **10**, 3178–3189.
92 M. Singh, N. Kaur, A. Casotto, L. Sangaletti and E. Comini, *Sensors Actuators B Chem.*, 2023, **384**, 133653.
93 N. Kaur, M. Singh and E. Comini, *Adv. Mater. Interfaces*, 2021, **n/a**, 2101629.
94 N. Kaur, M. Singh and E. Comini, *Langmuir*, 2020, **36**, 6326–6344.
95 N. Kaur, D. Zappa, V.-A. Maraloiu and E. Comini, *Adv. Funct. Mater.*, 2021, **n/a**, 2104416.
96 M. H. Raza, N. Kaur, E. Comini and N. Pinna, *Adv. Mater. Interfaces*, 2021, **8**, 2100939.
97 N. Kaur, M. Singh, A. Moumen, G. Duina and E. Comini, *Materials (Basel).*, 2020, 13.
98 D. Zappa, V. Galstyan, N. Kaur, H. M. M. Munasinghe Arachchige, O. Sisman and E. Comini, *Anal. Chim. Acta*, 2018.
99 J. Zhu, H. Wen, Y. Fan, X. Yang, H. Zhang, W. Wu, Y. Zhou and H. Hu, *Microchem. J.*, 2022, **181**, 107833.
100 M. W. G. Hoffmann, L. Mayrhofer, O. Casals, L. Caccamo, F. Hernandez-Ramirez, G. Lilienkamp, W. Daum, M. Moseler, A. Waag, H. Shen and J. D. Prades, *Adv. Mater.*, 2014, **26**, 8017–8022.
101 J.-L. Hou, C.-H. Wu and T.-J. Hsueh, *Sensors Actuators B Chem.*, 2014, **197**, 137–141.
102 R. Tanuma and M. Sugiyama, *Phys. status solidi*, 2019, **216**, 1800749.
103 M. Sturaro, E. Della Gaspera, N. Michieli, C. Cantalini, S. M. Emamjomeh, M. Guglielmi and A. Martucci, *ACS Appl. Mater. Interfaces*, 2016, **8**, 30440–30448.
104 N. Kaur, M. Singh, A. Casotto, L. Sangaletti and E. Comini, *Chem. Commun.*, 2023, **59**, 1329–1332.
105 M. Singh, N. Kaur, G. Drera, A. Casotto, L. S. Ermenegildo and E. Comini, *Adv. Funct. Mater.*, 2020, **30**, 2003217.

View Article Online
DOI: 10.1039/D4MA00426D

No primary research results, software or code have been included and no new data were generated or analysed as part of this review.